Predicting elastic strain fields in defective microstructures using image colorization algorithms

Pranav Milind Khanolkar [a], Christopher Carson McComb [a,b], Saurabh Basu [a,*]

[a] *Harold and Inge Marcus Department of Industrial and Manufacturing Engineering, Pennsylvania State University, University Park, PA, USA*
[b] *School of Engineering Design Technology and Professional Programs, Pennsylvania State University, University Park, PA, USA*

ARTICLE INFO

ABSTRACT

In this work, an image colorization algorithm based on convolutional neural networks is explored as an approach to predict tensile plane-strain field components of microstructures featuring porosity defects. For the same, microstructures featuring porosity of various shapes, sizes, area fractions and number densities were sampled on the gage section of ASTM-E8 sized numerical specimens whose tensile deformation was simulated in plane strain mode using commercial finite element analysis package Abaqus. Subsequently, the image colorization algorithm was trained by treating the microstructure featuring porosity defects as the gray scale image, and its strain field components as its color layers, analogous to the red-green-blue color components of traditional digital representations of images. Towards the same, various CNN frameworks were tested for optimization of its parameters, viz. number of layers, number of filters in each layer, stride, padding, and activation function. An optimized CNN framework is presented that is able to predict strain fields on randomly sampled microstructures with high accuracy $R^2 > 0.91$ at a fraction of the time that finite element analysis would take. Various cross-validation tests were performed to test the accuracy and robustness of the CNN in learning features of various microstructures. Results indicated that the CNN algorithm is extremely robust and can provide near-accurate strain fields in generic scenarios.

1. Introduction

The microstructure of a component plays an important role in governing its mechanical and functional properties. This realization has motivated research on various aspects of structure–function linkages with the overarching goal of instilling custom designed microstructures in components to endow them with superior response. These research efforts are backed by concomitant efforts towards process innovation that can produce these microstructures during fabrication or post-processing of the component geometry. Recently, additive manufacturing has garnered considerable interest as a tool for fabrication of complex geometries with custom designed microstructures. These processes often rely on computer software based slicing of a specified geometry for layer-by-layer fabrication. For the same, raw ingredients in powder or wire form are thermally activated and deposited onto a substrate that comprises the previously deposited slice. By spatially modulating the elemental composition of the raw ingredients and the dynamics of heat, complex microstructures can be produced additively that may not be accessible via traditional routes [1–5].

The integrity of additively produced microstructures can however be questionable due to its dependence on finely tuned thermal dynamics for producing error-free parts [6–8]. Fine tuning implies utilization of higher power inputs and slower scanning speeds. Unfortunately, slower throughput resulting from slower scanning speeds can overload the manufacturing system. However, intermediate and fast fabrication speeds that are deemed viable from the context of implementation naturally result in microstructure defects [9,10]. These defects include porosity/voids that are generated due to gas entrapment and lack of fusion, and compromise the performance of the microstructures, e.g. by shortening their life in fatigue-like loading conditions [11–13]. Additionally, additive manufacturing often relies on stochastic input raw material, i.e. metal powder. The sizes and shapes of individual particles in the powder are random, i.e. follow a distribution with a specified range and hence microstructures resulting from additive manufacturing can naturally contain stochastic imperfections including porosity/voids [14]. Finally, certain features in the geometry being fabricated additively may also promote formation of defects [15].

The traditional approach of eradicating microstructure defects in

* Corresponding author.
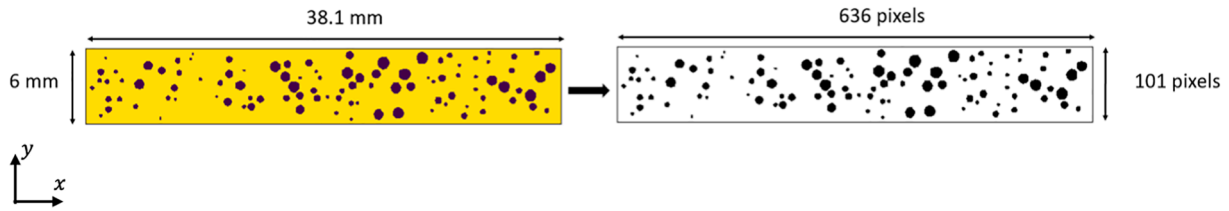*E-mail address:* sxb514@psu.edu (S. Basu).

Fig. 1. An example of microstructure converted to image (right) from ASTM-E8 specimen (left).

additively manufactured parts involves post-build hot isostatic pressing (HIP). However, the efficacy of HIP in eradicating all microstructure porosity/void defect remains < 1 [16,17]. For instance, HIP is ineffective at eradicating surface connected defects. These shortcomings recommend that designers exhibit judiciousness while planning use of additive manufacturing for creation of certain kinds of geometries, e.g. thin walled structures, that are especially prone to surface connected porosities.

The aforementioned shortcomings of additive manufacturing and post processing by HIP have motivated recent efforts in incorporating the combined effects of microstructure + defect structure + component geometry in making design decisions. Such frameworks enable revision of the design for making the defect structure that inevitably results from the manufacturing process tolerable. The challenges associated with this methodology involve computationally intensive simulations of several instances of multi-scale mechanics for achieving statistically significant insights and homogenization approaches to circumvent them have been proposed. Examples include the articles referenced in [18] where the effect of surface metrology defects on response of lattice structures is encapsulated within finite element framework using mechanically equivalent members. These members are designed using the distribution of observed metrology defects in real specimens. This methodology enables meshing of the simulated specimen with a much smaller number of elements, which accelerates the simulation. Analogous approaches have been utilized for accelerating discovery of composite microstructures that exhibit superior mechanical properties [19–22]. These efforts are often assisted by some variant of machine learning (ML) for bypassing finite element analysis in order to accelerate the discovery process.

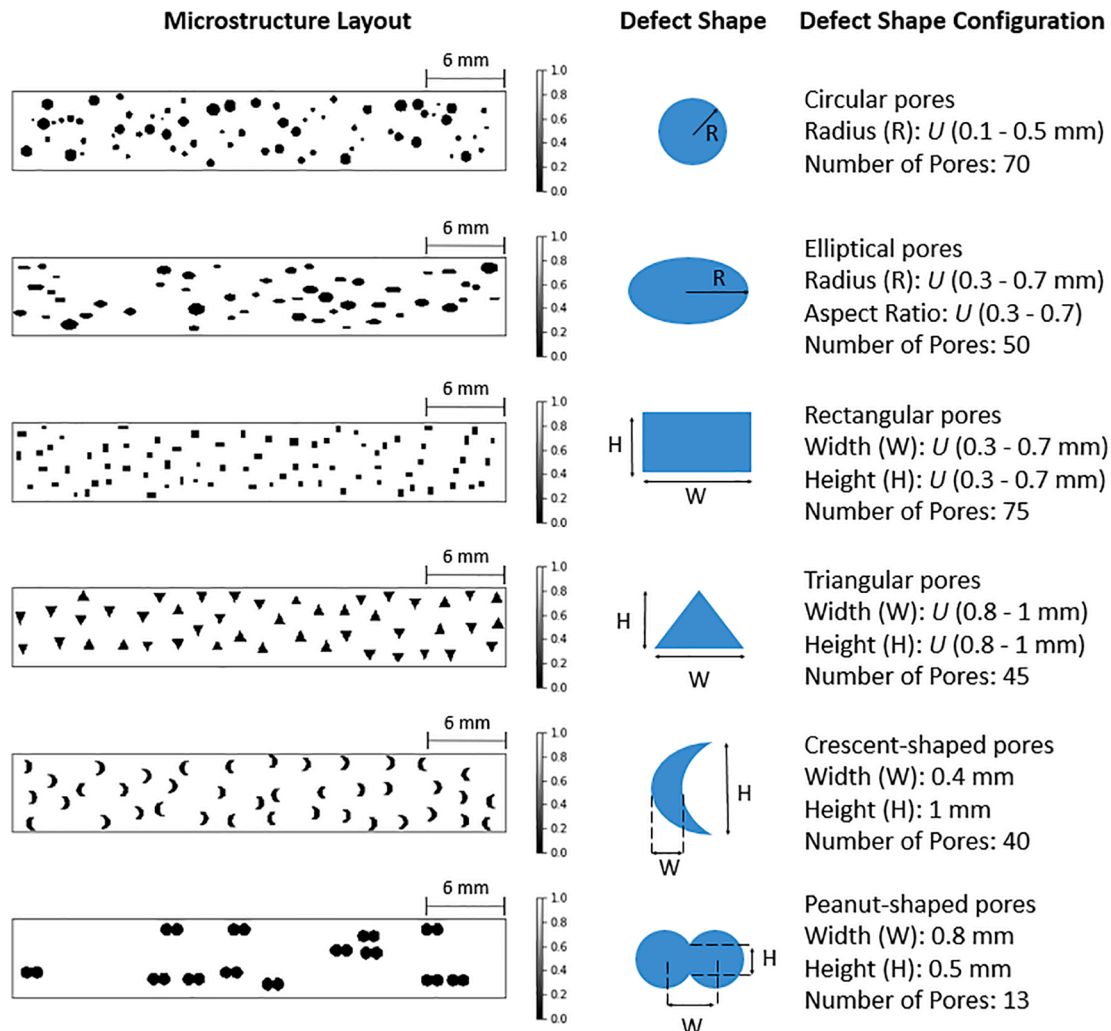The aforementioned ML based approaches strive to predict the mean

Fig. 2. Microstructure samples having different shapes of porosity defects with area fraction 7%–9%.
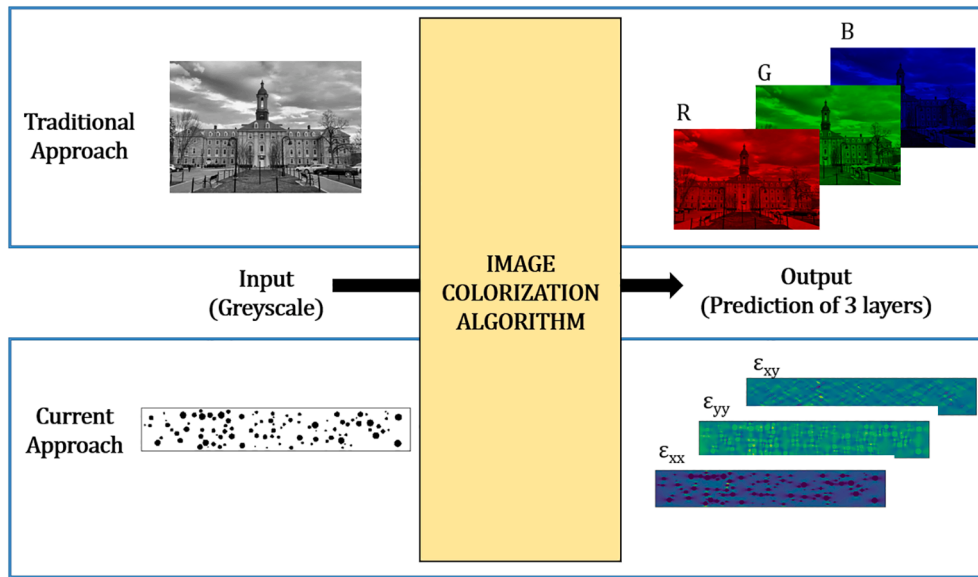
Fig. 3. Image Colorization Algorithm: Traditional and Current Approach.

response, e.g. volume averaged stress $\langle \sigma \rangle$ vs. strain $\langle \epsilon \rangle$ and force F vs. displacement d for characterizing the integrity of microstructure and design under various loading conditions. However, full field strains $\epsilon(\mathbf{x}, \mathbf{y})$ can provide valuable insights in complex scenarios where the spatial influence of microstructure features can create profound variations in mechanical response [23,24]. Previous approaches towards predicting strain fields using ML frameworks have looked at an extension of the materials knowledge system (MKS) that attempts to identify influence tensors $\alpha(\mathbf{r}, \mathbf{r}', ..., \mathbf{n}, \mathbf{n}', ...)$ [25]. This tensor encapsulates the effect of the presence of microstructure species $n, n', ...$ at relative locations $\mathbf{x} + \mathbf{r}, \mathbf{x} + \mathbf{r} + \mathbf{r}', ...$, on the central location $\mathbf{x}$, respectively. The roots of this approach can be traced back to works of Mura [26] and Beran [27].

In this article, ML based methodologies involving image colorization algorithms are explored for predicting strain fields for a pre-defined class of microstructures under specified boundary conditions. Conventional image colorization algorithms [28–30] comprise of artificial neural networks trained to predict three color-channels namely red, green and blue layers of an image from its greyscale layer. Well-trained artificial neural networks such as image colorization algorithms are known to predict results through feature/pattern recognition with high accuracy [31]. The gageability of artificial neural networks to recognize and capture features of data during its training stage have found its use in myriad applications such as image analyses [32–36], handwriting analyses [37,38], face detection or recognition [39,40], natural language processing [41,42] across different fields of science [43–45], engineering [46,47] and design [47–49]. This feature recognition ability has yielded tremendous results in their intended use for regression or classification of respective data. The hypothesis of this work includes prediction of the three strain fields components namely $\epsilon_{xx}(x, y), \epsilon_{yy}(x, y)$ and $\epsilon_{xy}(x, y)$ of a microstructure with porous defects can be done faster than traditional finite element analysis (FEA) software with significant accuracy using neural networks designed for image colorization. Microstructures featuring circular, elliptical and arbitrary shaped porosity defects in an elastic isotropic matrix are studied. Details of various aspects of this plan are described in Section 2.

2. Deformation simulation and machine learning framework

2.1. Sampling microstructures for deformation simulation

For the purpose of establishing a ML framework, microstructures $\mathcal{M}$

were sampled from a distribution and endowed to the gage section of a numerical ASTM-E8 tensile specimen [50] whose elastic response was simulated in the plane-strain mode using Abaqus standard. The microstructures $\mathcal{M}$ comprised an elastic isotropic matrix with $n_{\mathcal{D}} = 100$ circular porosity defects $\mathcal{D}$ whose diameters were uniformly distributed in the range $U(0.1 \; mm, 0.5 \; mm)$. Elasticity parameters corresponding to Al6061T6 alloy were used, i.e. Young's Modulus $E = 68.9 \; GPa$, Poisson's ratio $\nu = 0.35$. The material was assigned a density $\rho = 2700 \; Kgm^{-3}$. The microstructures were discretized onto a square grid as $\mathcal{M}(x, y)$ featuring x, y resolution ~$0.06 \; mm/pixel$ which produced $101 \times 636 \; pixel^2$ 2D microstructures as displayed in Fig. 1. The isotropic elastic matrix was assigned a value $\mathcal{M}(x, y) = 1 \; \forall \; (x, y) \notin \mathcal{D}$ and defect zones $\mathcal{D}$ were assigned values $\mathcal{M}(x, y) = 0 \; \forall \; (x, y) \in \mathcal{D}$. Tensile boundary conditions were imposed on the original (prior to discretization) specimen microstructure $\mathcal{M}$ featuring edge displacement $u_x = 0.1 \; mm$ corresponding to global strain ϵ_{xx}~0.003. The simulated response was quantified as strain field components $\epsilon_{xx}(x, y), \epsilon_{yy}(x, y)$, and $\epsilon_{xy}(x, y)$ that were extracted and discretized onto the same square grid as the microstructure $\mathcal{M}(x, y)$. Herein, zones within defects in these strain fields were assigned a value $\epsilon_{xx}(x, y) = 0, \epsilon_{yy}(x, y) = 0, \epsilon_{xy}(x, y) = 0 \; \forall \; (x, y) \in \mathcal{D}$. In this manner, 1000 samples of microstructures along with their strain field components were formed to assess the performance of the machine learning framework used in this work.

Microstructures with porosity defects comprising different shapes were also synthesized to evaluate the performance of the machine learning framework in terms of effective feature learning. The microstructures with their defect shapes and respective configurations, e.g. number count and dimensions, are displayed in Fig. 2. Herein, the number count was selected in a manner such that the total area fraction occupied by these defects $\mathcal{D}$ within the gauge section was between 7%–9%. These shapes comprise several two-dimensional (2D) geometric features such as a curved edge, straight edge, concave surface, and sharp corner, which are present in myriad complex microstructures. In this regard, these shapes were selected to facilitate thorough analysis of strain fields for evaluating feature learning characteristics of the machine learning framework. Locations of these microstructure features within the gauge section of the respective tensile specimens were uniformly distributed. Their corresponding discretized microstructure $\mathcal{M}(x, y)$ along with the corresponding strain fields $\epsilon_{xx}(x, y), \epsilon_{yy}(x, y), \epsilon_{xy}(x, y)$ also comprised inputs to the machine learning framework.

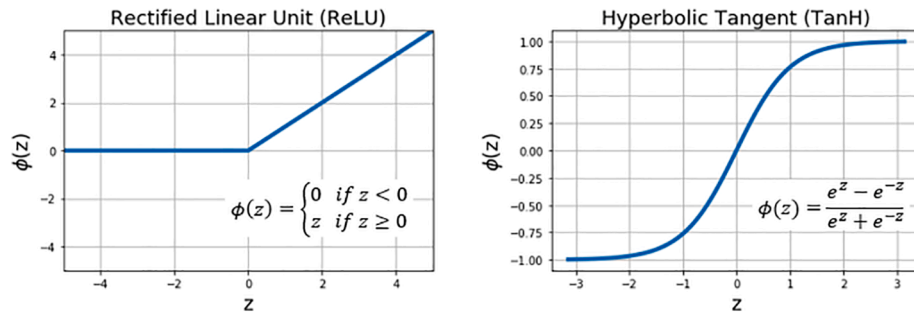The machine learning framework utilizes artificial neural networks,

Fig. 4. Activations Functions; ReLU and TanH.

specifically convolutional neural networks (CNNs) [31,51], wherein the inputs mentioned above are processed as images. The discretized microstructure $\mathscr{M}(x,y)$ are considered analogous to black and white images with the defect zones $\mathscr{D}$ represented by color 'black' and the area highlighting the material in the respective microstructure $\mathscr{M}(x,y)$ by color 'white'. The convolutional neural network implements the algorithm of image colorization to predict strain fields $\epsilon_{xx}(x,y), \epsilon_{yy}(x,y)$, and $\epsilon_{xy}(x,y)$ from the black and white image representing the given microstructure $\mathscr{M}(x,y)$.

2.2. Description of image colorization algorithm

An image comprises 2D arrays with values denoting pixel intensity. Black and white images or greyscale images consist of a single 2D array with values within a certain range with the two extremities of the range denoting black and white color respectively. In comparison, a colored image is formed by three layers, viz. red-green-blue (RGB), where each layer is a 2D array consisting of values representing the pixel intensity of the respective colors. In this context, convolutional neural networks [31,51] designed with the aim of colorizing black and white images utilize the concept of supervised machine learning wherein three layers (RGB) are predicted from a single layer black and white image and consequent stacking of these three layers together forms the colored image. This work utilizes image colorization by considering a microstructure $\mathscr{M}(x,y)$ with porosity defects as a greyscale input image and predicts the three strain fields components $\epsilon_{xx}(x,y), \epsilon_{yy}(x,y)$, and $\epsilon_{xy}(x, y)$ representing RGB output layers respectively, as illustrated in Fig. 3. Traditionally, an image colorization algorithm [28–30] functions by predicting colored version of a black and white image based on the weights stored in the hidden layers of the respective CNN developed, similar to a supervised machine learning implemented for basic regression models. Formulation of these weights in the CNN largely depends on the parameters defined during the development stage of the CNN. Appropriate selection and specification of the CNN parameters are highly crucial to achieve the prediction/output within a certain degree of accuracy. The parameters defined for the image colorization algorithm are described in the forthcoming sections.

CNN parameters such as input layer shape, kernel size, number of filters, padding, strides, activation function and optimizer were defined for the purpose of colorizing black and white microstructure images.

Specifying the shape of the array describing the black and white image is vital since the shape will remain constant throughout the CNN. The kernel/filter size defines the dimension of the weight matrix in each layer of the CNN. The kernel/filter size should be set suitably to account for the shape, size and location characteristics of the features within an image, in this case, the defect with largest radius and the proximity or position of the defects relative to each other. The number of filters in each layer are selected with the purpose of capturing maximum detail within an image. Even though the features within an image are easily captured by the filters specified in each layer of the CNN, details of the image around its edges are relatively harder to capture. In such instance, padding function within a layer is defined to account for the features and details around the edges of the image. The padding parameter when set at "same", will maintain the dimensions of the images (101×636 *pixel*^{2}; in this case) throughout the CNN layers. Strides within a CNN are specified to provide the magnitude of the movement of the filters across an image such that each pixel within an image is properly accounted for, e.g. stride = (1, 1) will enable the filter to move 1 pixel in horizontal and vertical direction. The activation functions serve to calculate the weights for each filter within a CNN layer. Apt activation function must be specified in each layer to compute the values of the weights set within respective CNN layer through which the image is transferred to the subsequent CNN layer. Rectified Linear (ReLU) activation functions were utilized throughout the CNN, except for the final two layers where Hyperbolic Tangent (TanH) activation function was specified to provide appropriate pixel values in accordance to the actual strain values. The activation functions used in the architecture are illustrated in Fig. 4. Adam optimizer [52] was selected to train the CNN and reconfigure the weights in each layer such that the error between the predicted output and the actual output is minimized. Suitable number of epochs are to be defined to train the network such that the feature details of the images are well-captured. The computation time and accuracy of the predicted results of such CNN mainly depend on these parameters and the number of layers specified in the CNN for a given hardware.

2.3. Implementation of image colorization for predicting strain fields

Image colorization was implemented in the Python programming language on a computer with a 2-core 6th Gen Intel Core i7-6500U processor, GeForce 940M GPU and 8 GB RAM using open source
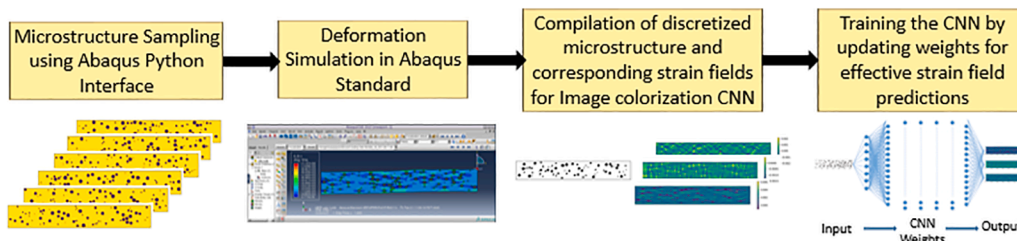

Fig. 5. Workflow.

Table 1
CNN architecture.

Layer No.	Layer Type	Parameter Specifications
0	Input Layer	Shape ($101 \times 636 \times 1$)
1	Conv. Layer	Filters: 4; Kernel size (9,9); Padding:"same"; Activation: ReLU; Strides: (1,1)
2	Conv. Layer	Filters: 4; Kernel size (9,9); Padding: "same", Activation: ReLU, Strides: (1,1)
3	Conv. Layer	Filters: 8; Kernel size (7,7); Padding: "same", Activation: ReLU, Strides: (1,1)
4	Conv. Layer	Filters: 8; Kernel size (7,7); Padding: "same", Activation: ReLU, Strides: (1,1)
5	Conv. Layer	Filters: 16; Kernel size (5,5); Padding: "same", Activation: ReLU, Strides: (1,1)
6	Conv. Layer	Filters: 16; Kernel size (5,5); Padding: "same", Activation: ReLU, Strides: (1,1)
7	Conv. Layer	Filters: 16; Kernel size (3,3); Padding: "same", Activation: ReLU, Strides: (1,1)
8	Conv. Layer	Filters: 16; Kernel size (3,3); Padding: "same", Activation: ReLU, Strides: (1,1)
9	Conv. Layer	Filters: 16; Kernel size (2,2); Padding: "same", Activation: ReLU, Strides: (1,1)
10	Conv. Layer	Filters: 16; Kernel size (2,2); Padding: "same", Activation: ReLU, Strides: (1,1)
11	Up-Sampling Layer	Size (1,1)
12	Conv. Layer	Filters: 16; Kernel size (2,2); Padding: "same", Activation: ReLU, Strides: (1,1)
13	Up-Sampling Layer	Size (1,1)
14	Conv. Layer	Filters: 8; Kernel size (3,3); Padding: "same", Activation: ReLU, Strides: (1,1)
15	Up-Sampling Layer	Size (1,1)
16	Conv. Layer	Filters: 4; Kernel size (7,7); Padding: "same", Activation: TanH, Strides: (1,1)
17	Up-Sampling Layer	Size (1,1)
18	Conv. Layer	Filters: 3; Kernel size (9,9); Padding: "same", Activation: TanH, Strides: (1,1)

machine learning frameworks: Keras (version 2.2.4) [53] and Tensorflow (version 1.13.1) [54]. The work flow illustrated in Fig. 5 involved: (i) sampling of microstructures using the python interface of Abaqus, (ii) numerical simulation of deformation using Abaqus standard, (iii) Compilation of discretized microstructure $\mathcal{M}(x, y)$ and strain field components $\epsilon_{xx}(x,y), \epsilon_{yy}(x,y), \epsilon_{xy}(x,y)$ as input to the image colorization module, (iv) updating of ML weights based on the Adam optimizer. Default parameters of this optimizer as listed in reference [52], viz. learning rate $\alpha = 0.001$, exponential decay rates $\beta_1 = 0.9$ and $\beta_2 = 0.999$ were chosen. The accuracy of the CNN architecture was computed in terms of average coefficient of determination R^2. A function that computes the coefficient of determination based on the predicted strain fields and corresponding actual strain fields was built using Python. The Keras library features a 'backend' function to perform low-level tensor manipulations such as computation of the sum of squares based on predicted and actual output values, which was used in this work for assessing the R^2 value. Herein, the R^2 value was obtained by comparing the predicted output and actual output, both represented by three strain field images ($\epsilon_{xx}(x,y), \epsilon_{yy}(x,y), \epsilon_{xy}(x,y)$) each. Several CNN architectures with varying number of convolutional layers and corresponding parameters described in the previous section were evaluated in terms of prediction time and accuracy. Increase in the number of convolutional layers, filters sizes and number of filters resulted in increase in time required for training the corresponding CNN and subsequently increased the time required to predict strain fields. The CNN architecture displayed in Table 1. was ultimately selected. The selection of this architecture was based on a tradeoff between the processing power of computer used, time required to predict results and accuracy of the results obtained.

Traditionally, a deep learning network, like the one used in this work, requires a considerable amount of data for training such that details in the respective datasets are captured and results are predicted with significant accuracy [55]. With this thought, the CNN was trained on 500 labeled samples for 100 iterations and tested on the rest 500 labeled samples of the 1000 microstructure dataset. This facilitated assessment of the performance of the CNN in comparison with Abaqus (FEA software) in terms of prediction time with significant accuracy. It must be noted that the accuracy of predicted strain fields of the microstructures largely depends on the finalized weights set by the training dataset of microstructures, each having different defect layout and size. Thus, different microstructures with different shape and size of defects coupled with their locations within the specimen will result in different accuracies during prediction of strain fields by the machine learning framework. These results are described in the results section along with experimental analyses highlighting the consistency in the performance of the CNN as well as its efficacy in learning various geometric features.

3. Results and discussion

This section describes the results obtained by the CNN shown in Table 1 in predicting elastic strain fields under given boundary conditions in microstructures with porous defects. The results are reported in three sub-sections, each exhibiting various benefits of this CNN. The first sub-section provides analysis of computation time and comparison of results between CNN and FEA. The second sub-section describes the effects of defect size and number on prediction times required by CNN and FEA. The third sub-section demonstrates the efficacy of CNNs in learning mechanistic aspects of various geometric shapes in the context of predicting their strain fields.
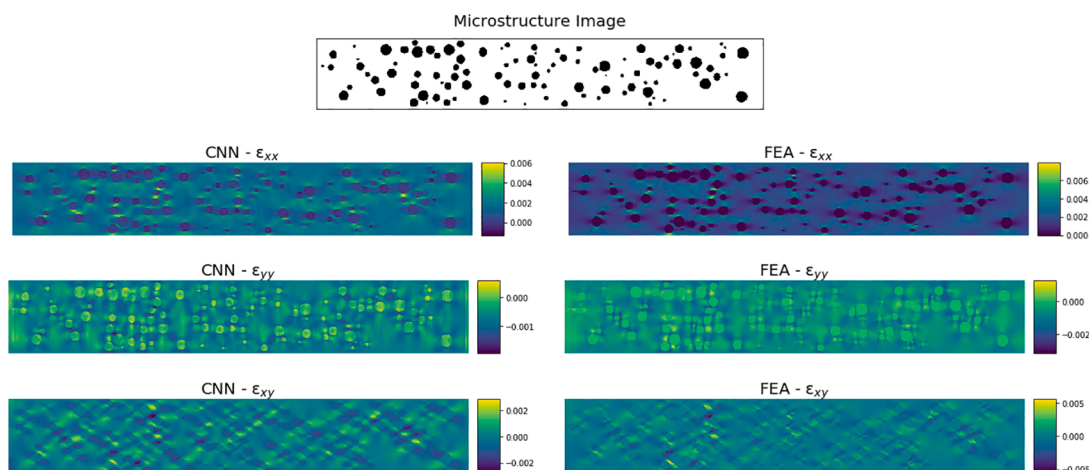

Fig. 6. Comparison of strain field predictions by CNN and FEA; R^2 value of CNN prediction: 95.77%.

Experiment 1: Varying size (radii - range) of pores;
No. of pores: 50 (constant)

Experiment 2: Varying number of pores;
Size (Radii - Range) of pores : *U (0.1 mm , 0.3 mm)* (constant)

Radii-Range : *U (0.15 mm, 0.2 mm)*

Number of pores: 20

Radii-Range : *U (0.3 mm, 0.35 mm)*

Number of pores: 80

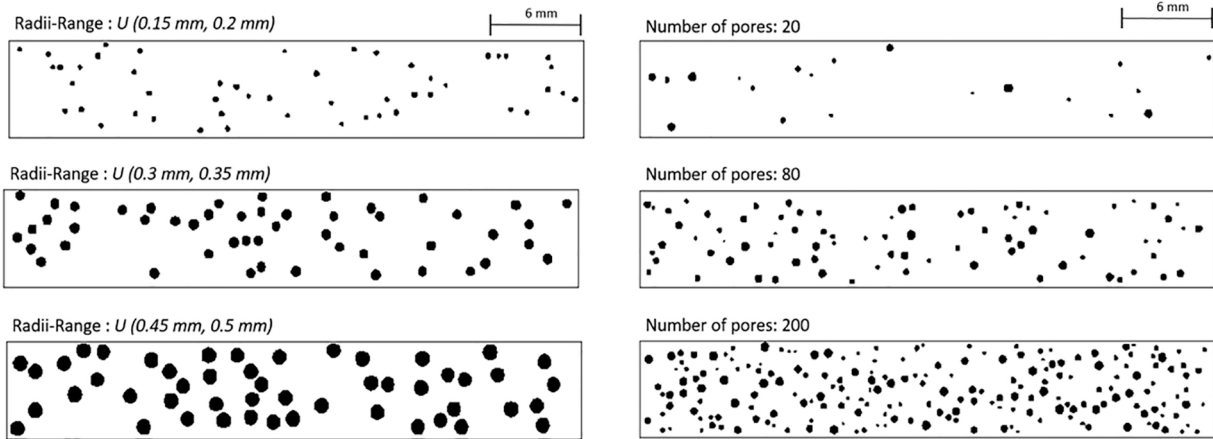Radii-Range : *U (0.45 mm, 0.5 mm)*

Number of pores: 200

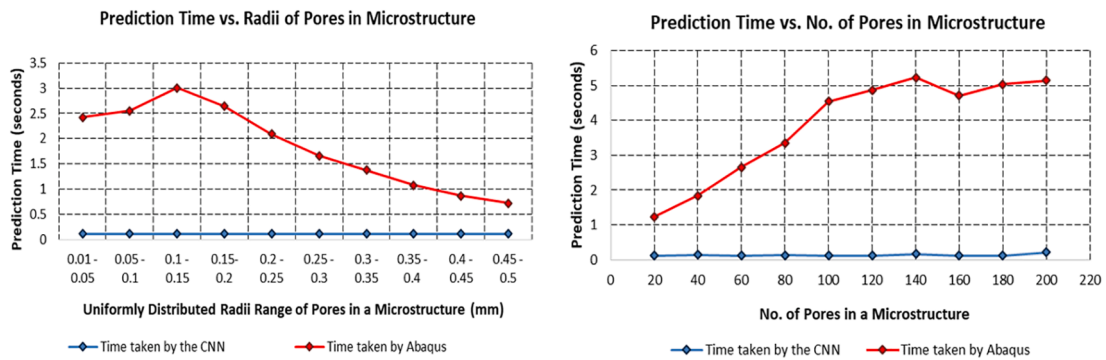**Fig. 7.** Microstructures examples for Experiment 1 (left) and Experiment 2 (right).

Fig. 8. Prediction time results obtained for Experiment 1 (left) and Experiment 2 (right).

3.1. Prediction time comparison: CNN vs. FEA

The CNN trained on 500 samples of microstructures with circular porous defects (No. of defects: 100; radius of the defects: $U(0.1\ mm,$ $0.5\ mm)$) provided a mean R^2 value 95.56% acquired from the 500 training datasets, using the GPU of the hardware utilized for training. The strain fields, $\epsilon_{xx}(x,y)$, $\epsilon_{yy}(x,y)$, and $\epsilon_{xy}(x,y)$, of a microstructure from the test dataset predicted by CNN, are illustrated in Fig. 6, along with the strain fields obtained from Abaqus (FEA). The strain fields for this particular microstucture are predicted with R^2 value of 95.77%,
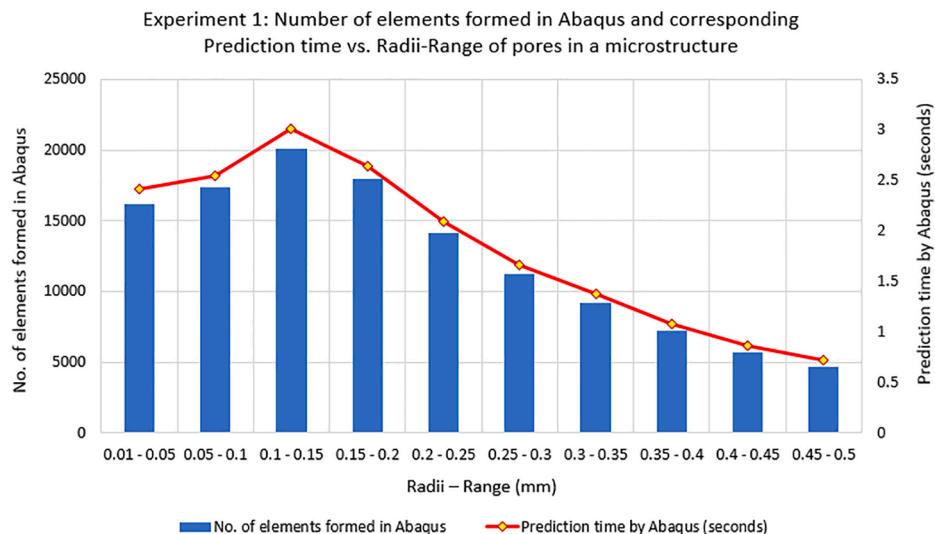
Fig. 9. Number of elements formed in the FEA software (Abaqus) for a given radii-range of pores within a microstructure.
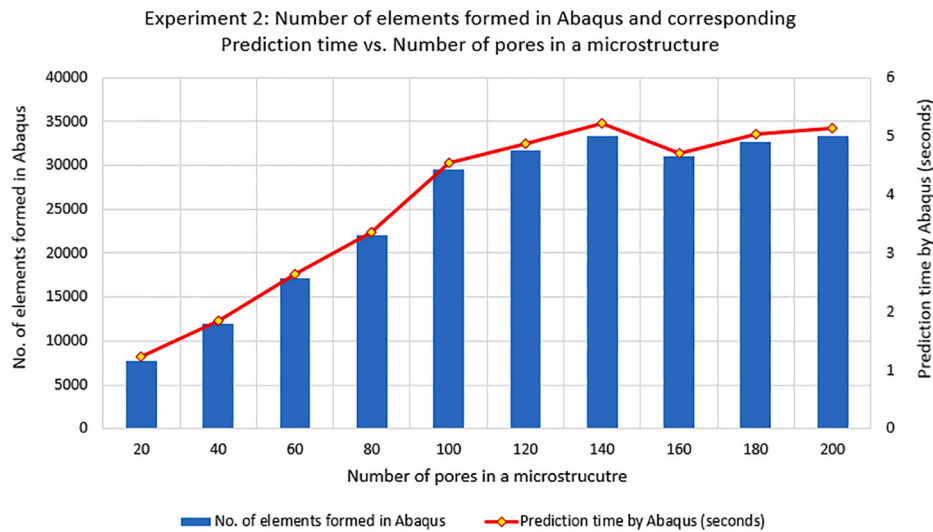
Fig. 10. Number of elements formed in the FEA software (Abaqus) for given number of defects within a microstructure.

using the CNN. 50 samples were selected randomly from the training dataset for prediction time comparison between the CNN and the original Abaqus simulation. The Abaqus simulation time considered in this work comprises only the problem solving time, following the microstructure modeling and meshing stages. The mean computation time required for Abaqus was found to be 2.23 ± 0.0433 s, while the CNN predicted the results in 0.13 ± 0.0171 s.

3.2. Experimental analyses: CNN vs. FEA

In order to further assess the efficacy of CNNs, 2 one-factor experiments were conducted to evaluate the performance of the CNN compared to Abaqus by varying the number and size of the porous defects in the microstructures. In the first experiment, the size of the pores in a microstructure was randomly varied from 0.01 mm to 0.5 mm in increments of 0.05 mm, each range distributed uniformly, with the number of pores kept constant at 50. In the second experiment, the size range of the porosity defects was kept constant between $U(0.1\ mm, 0.3\ mm)$ and the number of defects incremented from 20 till 200 in uniform increments of 20. Examples of the microstructures generated for these experiments are displayed in Fig. 7. The microstructure samples generated for these experiments were analyzed on the same CNN trained with microstructures having 100 circular pores of size range $U(0.1\ mm, 0.5\ mm)$.

The CNN was able to predict strain fields with mean coefficient of

determination R^2 values 95.26% and 94.11% for the first and second experiment, respectively. The results obtained through these experiments are depicted in Fig. 8. These results suggest that the CNN requires around 0.1 s - 0.2 s of prediction time, which does not change significantly with respect to radii and number of porosity defects. In contrast, prediction times exhibited by Abaqus are greatly influenced by radii and number of defects. These computation times were found to be positively correlated to the number of elements created during meshing as depicted in Figs. 9 and 10. In the first experiment, increase in the radii of the pores resulted in the formation of coarser mesh i.e. fewer elements are created during the meshing stage in FEA as depicted via the blue bars in Fig. 9. The formation of coarser mesh occurs due to decrease in the curvature of pores coupled with decrease in proximity of neighboring pores due to increase in their radii. In the second experiment, increase in the number of pores analogously resulted in an increase in the number of elements as depicted in Fig. 10. These variations can affect FEA computation times, e.g. by increasing the size of the global stiffness matrix that would then take longer to invert. However, in case of CNN used in this work, the prediction times observed were roughly uniform and dependent only on its architecture and parameters that were set during the training stage, and on the dimensions of the input image ($101 \times 636\ pixel^2$) of the microstructure whose strain fields are to be predicted.

Table 2
Coefficient of Determination R^2 Table for CNN Feature Learning Analysis.

Porosity-Defect Shapes of Test Dataset (50 samples)	Porosity-Defect Shapes of Training Dataset (500 samples)					
	Circle	Ellipse	Rectangle	Triangle	Crescent	Peanut
	Mean $R^2 \pm$ Std. Deviation	Mean $R^2 \pm$ Std. Deviation	Mean $R^2 \pm$ Std. Deviation	Mean $R^2 \pm$ Std. Deviation	Mean $R^2 \pm$ Std. Deviation	Mean $R^2 \pm$ Std. Deviation
Circle	0.9627 ± 0.0064	0.9272 ± 0.0097	0.8572 ± 0.0132	0.8775 ± 0.0070	0.9015 ± 0.0059	0.9401 ± 0.0056
Ellipse	0.9749 ± 0.0021	0.9703 ± 0.0029	0.9292 ± 0.0054	0.9167 ± 0.0021	0.9133 ± 0.0019	0.9699 ± 0.0015
Rectangle	0.8954 ± 0.0075	0.8899 ± 0.0080	0.9803 ± 0.0015	0.9329 ± 0.0023	0.8794 ± 0.0044	0.9289 ± 0.0055
Triangle	0.8973 ± 0.0039	0.8839 ± 0.0040	0.8959 ± 0.0039	0.9671 ± 0.0018	0.9113 ± 0.0030	0.8997 ± 0.0074
Crescent	0.8564 ± 0.0059	0.8174 ± 0.0068	0.7233 ± 0.0061	0.8459 ± 0.0064	0.9648 ± 0.0023	0.8187 ± 0.0065
Peanut	0.9657 ± 0.0091	0.9450 ± 0.0111	0.9147 ± 0.0103	0.9214 ± 0.0085	0.9230 ± 0.0064	0.9726 ± 0.0079

Low (R^2) (Color-scale for each column)   High (R^2)

Table 3
Coefficient of Determination R^2 Table for CNN trained on $\mathscr{M}(x,y)$ with all porosity-defect shapes.

Porosity-Defect Shapes of Test Dataset (50 samples)	CNN trained on datasets with 3000 microstructure samples of porosity defects shapes (circle + ellipse + rectangle + triangle + crescent + peanut)
	Mean R^2 ± Std. Deviation
Circle	0.9383 ± 0.0046
Ellipse	0.9350 ± 0.0030
Rectangle	0.9221 ± 0.0015
Triangle	0.9534 ± 0.0016
Crescent	0.9580 ± 0.0023
Peanut	0.9284 ± 0.0059

3.3. Feature learning analysis of CNN

Results described in the previous sub-section suggest that the CNN provides consistent and accurate predictions of strain fields in microsructures that feature circular porosity defects. In order to examine the learning ability of the CNN in more complex scenarios, six datasets each with 550 microstructure samples were synthesized, wherein each dataset comprised defects with unique shapes shown in Fig. 2. The CNN with same architecture and parameters as shown in Table 1 was trained on 500 samples of each dataset for 100 iterations, one at a time, and tested on the remaining 50 samples of every dataset. The performance of the CNN predictions was assessed by evaluating the R^2value in each case. Results from all six instances of training and testing the CNN are tabulated in Table 2 in terms of mean R^2 value and variability represented by its standard deviation. Herein, the vertical column on the left refers to the dataset that was used for training and the horizontal rows refer to datasets on which that CNN was tested.

From the diagonal in Table 2, it is apparent that the CNN trained on each of the six datasets can predict strain fields for microstructures with complex respective porosity shapes with significant accuracy R2 > 0.96. Further, it is observed from Table 2 that strain fields of microstructures in each of the six datasets are predicted with the CNN trained on elliptical or peanut shape pores consistently with reasonable accuracy $R^2 > 0.91$. Herein, the CNNs recognize the similarity in shape of elliptical pores and peanut-shaped pores and thus provide similar $R^{2}\sim 0.97$ value for predictions on their respective datasets when trained on the other. In comparison, the strain fields of microstructures with crescent-shaped pores are predicted with relatively less accuracy $R^2 < 0.87$, except the instance when tested with CNN trained on microstructures with crescent shaped pores itself. The reason for this behavior lies in the crescent pores' sharp concave shape, which is generally absent in every other shape studied here except the peanut. Herein, the rectangle represents a sharp convex shape that is least similar to the crescent $R^{2}\sim 0.72$ in the context of strain fields predicted in the former by the CNN that was trained using the latter. In the same vein, predictions made on CNN trained with microstructures with rectangular pores yields results with minimum $R^2 = 0.88$ for test dataset having microstructures with crescent pores.

In order to evaluate the overall consistency in predicting strain fields irrespective of shape of the defects, the CNN was trained on all of the aforementioned 3000 sample dataset. This trained CNN was tested on the 50 test samples from each of the six datasets and the results are illustrated in Table 3. It can be observed that the CNN trained using microstructures with different shapes of porous defects can predict strain fields with high accuracy $R^2 > 0.92$ in all cases. The CNN prediction of strain fields for one microstructure sample from each of the six datasets, along with its FEA counterpart is illustrated in Fig. 11. The

ability of CNNs to capture details are evident from the results wherein the strain fields predictions of microstructures with porous defects are made with significant accuracy highlighting strain concentrations at appropriate locations, regardless of the defect-shapes.

4. Conclusion and future work

The following conclusions could be drawn from this work:

1. A CNN based image colorization algorithm was tested as an approach to predict elastic strain fields in microstructures with porosity defects of various shapes when subject to a specified boundary condition. The CNN was trained by sampling instances of microstructures in the gage section of ASTME8 sized specimen and simulating their elastic deformation in the plane strain mode using the commercial FEA package Abaqus. For the same, microstructures were treated as gray scale images and their strain field components were treated as color components. It was seen that the image colorization algorithm is able to predict strain fields with high accuracy in a fraction of the time taken by FEA software. Reasons for faster speeds via CNN included deterministic processes, viz. CNN architecture and parameters that do not change as long as the size of the input raw image is maintained. Reasons for slower speeds in FEA calculations include its dependence on the size of the mesh. Finer microstructures were generally found to produce denser meshes comprising a larger number of elements over equivalent areas that resulted in slower albeit more accurate processing by FEA.
2. Computational analyses was performed to evaluate the ability of the image colorization algorithms in learning features of various shapes with respect to prediction of strain fields under specified boundary conditions. The CNN based framework could successfully predict highly accurate $R^2 > 0.91$ strain fields in microstructures, irrespective of the shape of defects.

The strain fields predicted in this research pertain to microstructures with a specific material, having specific elastic properties and a uniform boundary condition. This limits the CNN to predict strain fields for microstructures with the aforementioned conditions. In addition to that, training the CNN takes considerable amount of time and power which depends on the hardware used for this purpose. Complications in CNN predictions may arise in instances where defect-shapes differ significantly from those the CNN was trained on. For example, the effect of concavity in peanut-shaped defects is almost negligible since the geometric aspect of concavity present in those shapes is considerably small compared to the overall shape of the defects; increase in such concave aspects of the defects may result in predictions that are less accurate those obtained by FEA software. Further, the current work can accurately make strain field predictions for microstructures with only porosity defects. Structural analyses of microstructures with features such as inclusions of myriad sizes and material compositions can be possible by appropriate retraining of CNN and will be addressed in future work.

5. Data availability

All data generated for research in this article is available from the Mendeley open access data repositories [56–58].

Declaration of Competing Interest

The authors declare that they have no known competing financial interests or personal relationships that could have appeared to influence the work reported in this paper.
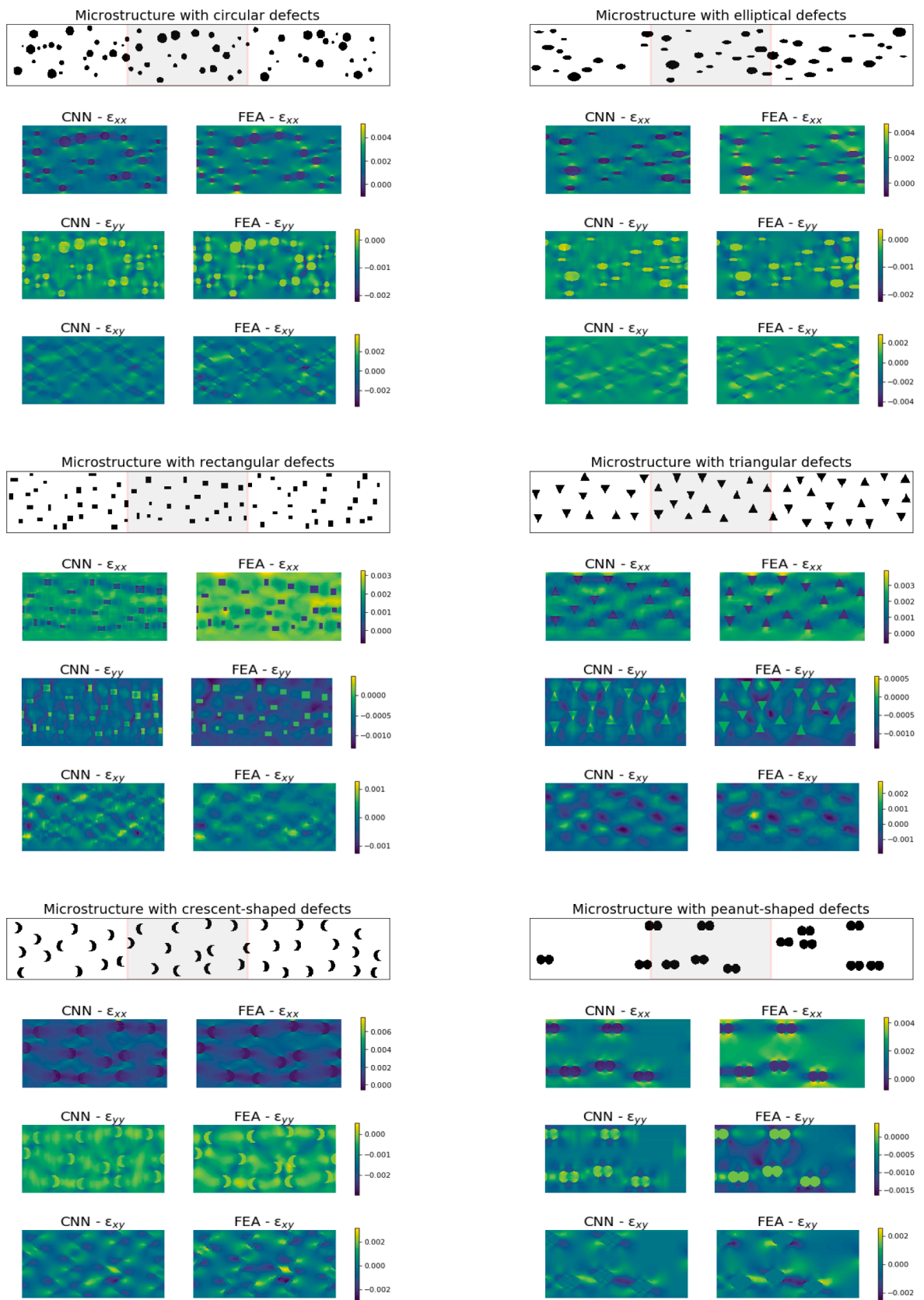
Fig. 11. Strain field predictions of the zones highlighted in microstructures with different defect shapes.

Acknowledgements

References

[1] Theron M. Rodgers, Hojun Lim, Judith A. Brown, Three-dimensional additively manufactured microstructures and their mechanical properties, JOM (2019).

[2] Minh-Son Pham, Chen Liu, Iain Todd, Jedsada Lertthanasarn, Damage-tolerant architected materials inspired by crystal microstructure, Nature 565 (7739) (2019) 305–311.

[3] Andrew T. Polonsky, William C. Lenthe, McLean P. Echlin, Veronica Livescu, George T. Gray, Tresa M. Pollock, Solidification-driven orientation gradients in additively manufactured stainless steel, Acta Materialia 183 (2020) 249–260.

[4] P.C. Collins, D.A. Brice, P. Samimi, I. Ghamarian, H.L. Fraser, Microstructural control of additively manufactured metallic materials, Annual Review of Materials Research 46 (1) (2016) 63–91.

[5] J.S. Zuback, T.A. Palmer, T. DebRoy, Additive manufacturing of functionally graded transition joints between ferritic and austenitic alloys, Journal of Alloys and Compounds 770 (2019) 995–1003.

[6] T. Mukherjee, J.S. Zuback, W. Zhang, T. DebRoy, Residual stresses and distortion in additively manufactured compositionally graded and dissimilar joints, Computational Materials Science 143 (2018) 325–337.

[7] G. Vastola, G. Zhang, Q.X. Pei, Y.-W. Zhang, Controlling of residual stress in additive manufacturing of ti6al4v by finite element modeling, Additive Manufacturing 12 (2016) 231–239 (Special Issue on Modeling and Simulation for Additive Manufacturing).

[8] T. Mukherjee, T. DebRoy, Mitigation of lack of fusion defects in powder bed fusion additive manufacturing, Journal of Manufacturing Processes 36 (2018) 442–449.

[9] Qian Chu Liu, Joe Elambasseril, Shou Jin Sun, Martin Leary, Milan Brandt, Peter Khan Sharp, The effect of manufacturing defects on the fatigue behaviour of ti-6al-4v specimens fabricated using selective laser melting, in: 11th International Fatigue Congress, volume 891 of Advanced Materials Research, pp. 1519–1524. Trans Tech Publications Ltd, 5 2014.

[10] Lore Thijs, Frederik Verhaeghe, Tom Craeghs, Jan Van Humbeeck, Jean-Pierre Kruth, A study of the microstructural evolution during selective laser melting of ti–6al–4v, Acta Materialia 58 (9) (2010) 3303–3312.

[11] S. Tammas Williams, P.J. Withers, I. Todd, P.B. Prangnell, The influence of porosity on fatigue crack initiation in additively manufactured titanium components, Scientific Reports 7 (2017) (7308).

[12] Junwen Zhao, Mark Easton, Ma. Qian, Martin Leary, Milan Brandt, Effect of building direction on porosity and fatigue life of selective laser melted alsi12mg alloy, Materials Science and Engineering: A 729 (2018) 76–85.

[13] Panding Wang, Hongshuai Lei, Xiaolei Zhu, Haosen Chen, Daining Fang, Influence of manufacturing geometric defects on the mechanical properties of alsi10mg alloy fabricated by selective laser melting, Journal of Alloys and Compounds 789 (2019) 852–859.

[14] Haijun Gong, Khalid Rafi, Hengfeng Gu, Thomas Starr, Brent Stucker, Analysis of defect generation in ti–6al–4v parts made using powder bed fusion additive manufacturing processes, Additive Manufacturing, 1–4 (2014) 87–98 (Inaugural Issue).

[15] Niloofar Sanaei, Ali Fatemi, Nam Phan, Defect characteristics and analysis of their variability in metal l-pbf additive manufacturing, Materials and Design 182 (2019), 108091.

[16] Samuel Tammas-Williams, Philip J. Withers, Iain Todd, Philip B. Prangnell, The effectiveness of hot isostatic pressing for closing porosity in titanium parts manufactured by selective electron beam melting, Metallurgical and Materials Transactions A 47 (5) (2016) 1939–1946.

[17] S. Tammas-Williams, P.J. Withers, I. Todd, P.B. Prangnell, Porosity regrowth during heat treatment of hot isostatically pressed additively manufactured titanium components, Scripta Materialia 122 (2016) 72–76.

[18] Lu. Liu, Paul Kamm, Francisco García-Moreno, John Banhart, Damiano Pasini, Elastic and failure response of imperfect three-dimensional metallic lattices: The role of geometric defects induced by selective laser melting, Journal of the Mechanics and Physics of Solids 107 (2017) 160–184.

[19] Jaimyun Jung, Jae Ik Yoon, Hyung Keun Park, Jin You Kim, Hyoung Seop Kim, An efficient machine learning approach to establish structure-property linkages, Computational Materials Science 156 (2019) 17–25.

[20] Ruoqian Liu, Abhishek Kumar, Zhengzhang Chen, Ankit Agrawal, Veera Sundararaghavan, Alok Choudhary, An efficient machine learning approach to establish structure-property linkages, Scientific Reports 5 (2015) 11551.

[21] Chun-Teh Chen, X.Gu. Grace, Effect of constituent materials on composite performance: exploring design strategies via machine learning, Advanced Theory and Simulations 2 (6) (2019) 1900056.

[22] Zhi-Lei Wang, Toshio Ogawa, Yoshitaka Adachi, A machine learning tool for materials informatics, Advanced Theory and Simulations, n/a(n/a) (2019) 1900177.

[23] Joseph Bartolai, Alexander E. Wilson-Heid, Jordan R. Kruse, Allison M. Beese, Timothy W. Simpson, Full field strain measurement of material extrusion additive

[24] manufacturing parts with solid and sparse infill geometries, JOM 71 (3) (2019) 871–879.

[24] Mohsen Seifi, Ayman Salem, Daniel Satko, Joshua Shaffer, John J. Lewandowski, Defect distribution and microstructure heterogeneity effects on fracture resistance and fatigue behavior of ebm ti–6al–4v. International Journal of Fatigue, 94 (2017) 263–287 (Fatigue and Fracture Behavior of Additive Manufactured Parts).

[25] Yuksel C. Yabansu, Surya R. Kalidindi, Representation and calibration of elastic localization kernels for a broad class of cubic polycrystals, Acta Materialia 94 (2015) 26–35.

[26] T. Mura, Micromechanics of Defects in Solids. Mechanics of Elastic and Inelastic Solids, Springer, Netherlands, 1987.

[27] M. Beran, Statistical Continuum Theories. Interscience Publisher, 1968.

[28] Federico Baldassarre, Diego González Morín, Lucas Rodés-Guirao, Deep koalarization: Image colorization using cnns and inception-resnet-v2. arXiv preprint arXiv:1712.03400, 2017.

[29] Richard Zhang, Phillip Isola, Alexei A. Efros, Colorful image colorization, in: European Conference on Computer Vision, Springer, 2016, pp. 649–666.

[30] Zezhou Cheng, Qingxiong Yang, Bin Sheng, Deep colorization, in: Proceedings of the IEEE International Conference on Computer Vision, 2015, pp. 415–423.

[31] Keiron O'Shea, Ryan Nash, An introduction to convolutional neural networks, arXiv preprint arXiv:1511.08458, 2015.

[32] Aritra Chowdhury, Elizabeth Kautz, Bülent Yener, Daniel Lewis, Image driven machine learning methods for microstructure recognition, Computational Materials Science (2016).

[33] Xu. Yan, Tao Mo, Qiwei Feng, Peilin Zhong, Maode Lai, Eric I. Chao Chang, Deep learning of feature representation with multiple instance learning for medical image analysis, ICASSP, IEEE International Conference on Acoustics, Speech and Signal Processing – Proceedings (2014).

[34] Tsung Han Chan, Kui Jia, Shenghua Gao, Jiwen Lu, Zinan Zeng, Yi Ma, PCANet: A simple deep learning baseline for image classification? IEEE Transactions on Image Processing, 2015.

[35] Muhammad Imran Razzak, Saeeda Naz, Ahmad Zaib, Deep learning for medical image processing: overview, challenges and the future, in: Lecture Notes in Computational Vision and Biomechanics, Springer, 2018.

[36] Naiyan Wang, Dit Yan Yeung, Learning a deep compact image representation for visual tracking, in: Advances in Neural Information Processing Systems, 2013.

[37] Li Deng, The MNIST database of handwritten digit images for machine learning research, IEEE Signal Processing Magazine (2012).

[38] Durjoy Sen Maitra, Ujjwal Bhattacharya, Swapan K. Parui< CNN based common approach to handwritten character recognition of multiple scripts, in: Proceedings of the International Conference on Document Analysis and Recognition, ICDAR, 2015.

[39] Bogdan Kwolek, Face detection using convolutional neural networks and gabor filters, in: Lecture Notes in Computer Science (including subseries Lecture Notes in Artificial Intelligence and Lecture Notes in Bioinformatics), 2005.

[40] Stan Z. Li, Juwei Lu, Face recognition using the nearest feature line method, IEEE Transactions on Neural Networks, 1999.

[41] Tom Young, Devamanyu Hazarika, Soujanya Poria, Erik Cambria, Recent trends in deep learning based natural language processing [Review Article], 2018.

[42] Honglak Lee, Largman Yan, Peter Pham, Andrew Y. Ng, Unsupervised feature learning for audio classification using convolutional deep belief networks, in: Advances in Neural Information Processing Systems 22 – Proceedings of the 2009 Conference, 2009.

[43] Garrett B. Goh, Nathan O. Hodas, Abhinav Vishnu, Deep learning for computational chemistry, 2017.

[44] Travers Ching, Daniel S. Himmelstein, Brett K. Beaulieu-Jones, Alexandr A. Kalinin, Brian T. Do, Gregory P. Way, Enrico Ferrero, Paul Michael Agapow, Michael Zietz, Michael M. Hoffman, Wei Xie, Gail L. Rosen, Benjamin J. Lengerich, Johnny Israeli, Jack Lanchantin, Stephen Woloszynek, Anne E. Carpenter, Avanti Shrikumar, Jinbo Xu, Evan M. Cofer, Christopher A. Lavender, Srinivas C. Turaga, Amr M. Alexandari, Zhiyong Lu, David J. Harris, Dave Decaprio, Yanjun Qi, Anshul Kundaje, Yifan Peng, Laura K. Wiley, Marwin H.S. Segler, Simina M. Boca, S. Joshua Swamidass, Austin Huang, Anthony Gitter, Casey S. Greene, Opportunities and obstacles for deep learning in biology and medicine, Journal of the Royal Society Interface, 2018.

[45] P. Baldi, P. Sadowski, D. Whiteson, Searching for exotic particles in high-energy physics with deep learning, Nature Communications (2014).

[46] Christopher McComb, Toward the rapid design of engineered systems through deep neural networks, in: Design Computing and Cognition '18, Springer, 2019.

[47] Glen Williams, Nicholas A. Meisel, Timothy W. Simpson, Christopher McComb, Design repository effectiveness for 3D convolutional neural networks: application to additive manufacturing, Journal of Mechanical Design 141 (11) (2019) 1–12.

[48] Christopher McComb, Christian Murphey, Nicholas Meisel, Timothy W. Simpson, Predicting part mass, required support material, and build time via autoencoded voxel patterns, in: 29th Annual International Solid Freeform Fabrication Symposium, 2018.

[49] Ayush Raina, Christopher McComb, Jonathan Cagan, Learning to design from humans: imitating human designers through deep learning, Journal of Mechanical Design 141 (11) (2019) 1–11.

[50] Transportation Officials Standard, An American, and National Standard, ASTM E8M-13a. ASTM, 2014, pp. 1–28.

[51] Jianxin Wu, Introduction to convolutional neural networks. National Key Lab for Novel Software Technology. Nanjing University. China, 5:23, 2017.

[52] Diederik P. Kingma, Jimmy Lei Ba, Adam: A method for stochastic optimization, in: 3rd International Conference on Learning Representations, ICLR 2015 - Conference Track Proceedings, 2015.

[53] François Chollet et al. Keras. https://keras.io, 2015.

[54] Martín Abadi, Paul Barham, Jianmin Chen, Zhifeng Chen, Andy Davis, Jeffrey Dean, Matthieu Devin, Sanjay Ghemawat, Geoffrey Irving, Michael Isard, et al., Tensorflow: A system for large-scale machine learning. In 12th USENIX Symposium on Operating Systems Design and Implementation (OSDI 16), 2016, pp. 265–283.

[55] W. Sha, K.L. Edwards, The use of artificial neural networks in materials science based research, 2007.

[56] Pranav Milind Khanolkar, Saurabh Basu, Christopher McComb, Image-based data on strain fields of microstructures with porosity defects-1, https://doi.org/10.17632/s4g76zd5ys.1.

[57] Pranav Milind Khanolkar, Saurabh Basu, Christopher McComb, Image-based data on strain fields of microstructures with porosity defects-2, https://doi.org/10.17632/jkkbg4d49g.1.

[58] Pranav Milind Khanolkar, Saurabh Basu, Christopher McComb, Image-based data on strain fields of microstructures with porosity defects-3, https://doi.org/10.17632/ns4bby8s6m.1.